nuclear fusion
IAEA

PAPER • OPEN ACCESS

Exploring the role of topography in the sputtering process of tungsten by GyM helium plasma

To cite this article: Andrea Uccello *et al* 2025 *Nucl. Fusion* **65** 056006

OPEN ACCESS
IOP Publishing | International Atomic Energy Agency
Nuclear Fusion
Nucl. Fusion **65** (2025) 056006 (17pp)
https://doi.org/10.1088/1741-4326/adc3aa

Exploring the role of topography in the sputtering process of tungsten by GyM helium plasma

Andrea Uccello[1,*], Gabriele Alberti[2], Matteo Pedroni[1], Anna Cremona[1], Francesco Ghezzi[1], Miriam Saleh[1], Espedito Vassallo[1], Luigi Bana[2], David Dellasega[1,2], Matteo Passoni[1,2], Carlo Tuccari[2], Davide Vavassori[2], Antti Hakola[3], Marcin Rasinski[4], Juri Romazanov[4] and the GyM Team[a]

[1] Istituto per la Scienza e Tecnologia dei Plasmi, CNR, 20125 Milan, Italy
[2] Dipartimento di Energia, Politecnico di Milano, 20133 Milan, Italy
[3] VTT Technical Research Centre of Finland Ltd, PO Box 1000, Espoo FI-02044 VTT, Finland
[4] Forschungszentrum Jülich GmbH, Institut für Energie-und Klimaforschung-Plasmaphysik, Partner of the Trilateral Euregio Cluster (TEC), 52425 Jülich, Germany

E-mail: andrea.uccello@istp.cnr.it

Received 10 January 2025, revised 12 March 2025
Accepted for publication 21 March 2025
Published 1 April 2025

Abstract

This work investigates the role of surface topography in the sputtering process of tungsten (W) exposed to helium plasma using the GyM linear device. Surfaces with varying roughness, from sub-nanometer to approximately 1 μm, and different textures, including random-like and regular configurations, were studied. The samples were exposed to helium plasma of GyM at energies ranging from 30 to 350 eV, with a fluence of $\approx 4.3 \times 10^{24}$ $He^{+}m^{-2}$ and temperatures well below the bulk W fuzz formation threshold of ≈700 °C. The interpretation of the experimental results was supported by simulations with the 3D Monte Carlo ERO2.0 code. Analysis with atomic force and scanning electron microscopy revealed that surface topography remained largely unchanged, while a nanoscale undulating surface structure formed on all samples at the highest incident energies. The effective sputtering yield (Y_{eff}) of tungsten, derived from mass and thickness loss data, was consistently lower than predictions from simulations by up to an order of magnitude, likely due to the dynamic retention of helium on the tungsten surface. On the other hand, both experimental results and modelling agree that surface topography's influence on sputtering can be entirely captured by the average surface inclination angle (δ_m), which unequivocally characterises each specimen, unlike the average roughness (R_a). Moreover, Y_{eff} values from both mass loss data and ERO2.0 simulations as a function of δ_m align well with a decreasing sigmoid fit function. A reduction of more than 50% was observed when comparing the flat surface to that with the highest R_a, attributed by ERO2.0 to the increasing fraction of sputtered tungsten atoms being deposited on neighbouring surfaces. These findings underscore the importance of accurately calibrating simulation tools against linear plasma device

[a] See Uccello *et al* 2023 (https://doi.org/10.3389/fphy.2023.1108175) for the GyM Team.
[*] Author to whom any correspondence should be addressed.

experiments for predicting the lifetime of plasma-facing components in fusion reactors such as ITER and DEMO, emphasising the potential of structured tungsten surfaces to reduce erosion and impurity concentration in the plasma core.

Keywords: GyM, linear plasma device, tungsten, helium plasma, sputtering, topography, plasma–wall interaction

(Some figures may appear in colour only in the online journal)

1. Introduction

In magnetically confined fusion reactors designed for deuterium–tritium reactions, such as ITER and the demonstration power plant DEMO, the plasma-facing components (PFCs) of both the divertor and the main chamber must withstand a wide range of harsh conditions in terms of particle fluxes, energies, and heat loads. In particular, ion fluxes of $\leqslant 1 \times 10^{25}$ m^{-2} s^{-1}, with typical energies of a few tens of eV, along with a nominal heat load of 10 MW m^{-2}, are expected on the divertor tiles of ITER during steady-state operation [1]. Even in the main chamber, the PFCs will be exposed to considerable heat loads of $\approx$1.0 MW m^{-2} and particle fluxes between 1×10^{20} and 1×10^{22} m^{-2} s^{-1}, including energetic charge-exchange neutrals and radially diffusing plasma ions from the scrape-off layer, with energies reaching the keV range [2, 3]. The incident particles will consist of fuel hydrogen isotopes, helium (He) ash produced from deuterium–tritium nuclear fusion reactions, and other impurities. The resulting plasma–material interactions will lead to significant modifications of the PFCs, including sputtering, blistering, and the formation of nanostructures on their surfaces, which will ultimately result in the degradation of their mechanical and thermal properties, thereby inevitably affecting their lifetime [4].

Due to its low sputtering yield, high melting point, excellent thermal conductivity, low hydrogen retention, and manageable levels of induced radioactivity, tungsten (W) is recognised as the primary candidate for the PFCs in both the divertor and main chamber of ITER and DEMO [5, 6]. Over the past two decades, extensive research has been conducted on W as a plasma-facing material, covering both theoretical and experimental aspects [7, 8]. A key finding from these studies is the crucial role that helium plays in the interaction between the plasma and the W surface, which leads, for instance, to the formation of the well-known fuzz nanostructures [9–15].

This work explores the physics of tungsten erosion by helium under conditions relevant to the main chamber of ITER and DEMO. The GyM linear plasma device [16, 17] was used for this purpose, as it can achieve ion fluxes of $\leqslant 1 \times 10^{21}$ m^{-2} s^{-1} and energies reaching 400 eV (by applying a negative bias voltage to its sample holder), effectively simulating the plasma–wall interaction (PWI) outside the divertor region. The focus is here on the influence of surface topography, which has been shown to significantly affect the effective sputtering yield [18–21]. The aim is to comprehensively address this topic by considering surfaces with varying roughness, from the sub-nanometer range up to $\sim$1 μm, which is the typical order of magnitude for the roughness of fresh PFCs [22], as well as textures that span from irregular, random-like surfaces to more regular surfaces with specific features. This study extends the existing literature on experiments conducted with other linear machines [20] and ion beam sputtering facilities [21]. The interpretation of the experimental results from the exposure of W samples to the GyM He plasma was supported by simulations with ERO2.0, a 3D Monte Carlo code that can investigate material erosion by plasma, as well as the transport and deposition of released impurities at both global and local microscopic scales [20, 23–25]. In this contribution, ERO2.0 simulations incorporating the surface morphology model were performed to account for the effect of surface roughness and texturing on W erosion [20, 25].

This paper is organised as follows. The preparation and characterisation of tungsten samples, along with the exposure conditions to GyM helium plasma, are discussed in section 2. The ERO2.0 modelling framework is described in section 3. Results from both the experiments and ERO2.0 simulations, together with their interpretation, are presented in section 4. A summary, as well as considerations from the perspective of PWI in tokamaks and future developments, is provided in section 5.

2. Experimental

For the experiments, samples with a different topography were considered. In particular, compact tungsten coatings, 500 nm thick, were deposited by high-power impulse magnetron sputtering (HiPIMS) on top of fine-grained graphite (Gr) and silicon (Si) substrates featuring different texturing and average roughness (R_a). Polished bulk W samples fulfilling ITER specifications, used in the frame of the EUROfusion PWI & Exhaust Work-Package activities, were also included in the study as reference [4].

The topography of the samples was investigated before and after W film deposition, as well as at the end of the exposures to the GyM plasma, using a Core atomic force microscope (AFM) from Nanosurf GmbH (Langen, Germany), operating in ambient air and dynamic mode with a Dyn190Al probe (force constant 28–75 N m^{-1} and tip radius 10 nm). Three AFM images on a scan area of 50×50 μm^2 were acquired to evaluate surface roughness parameters, like R_a and the mean surface inclination angle δ_m, with the Gwyddion open

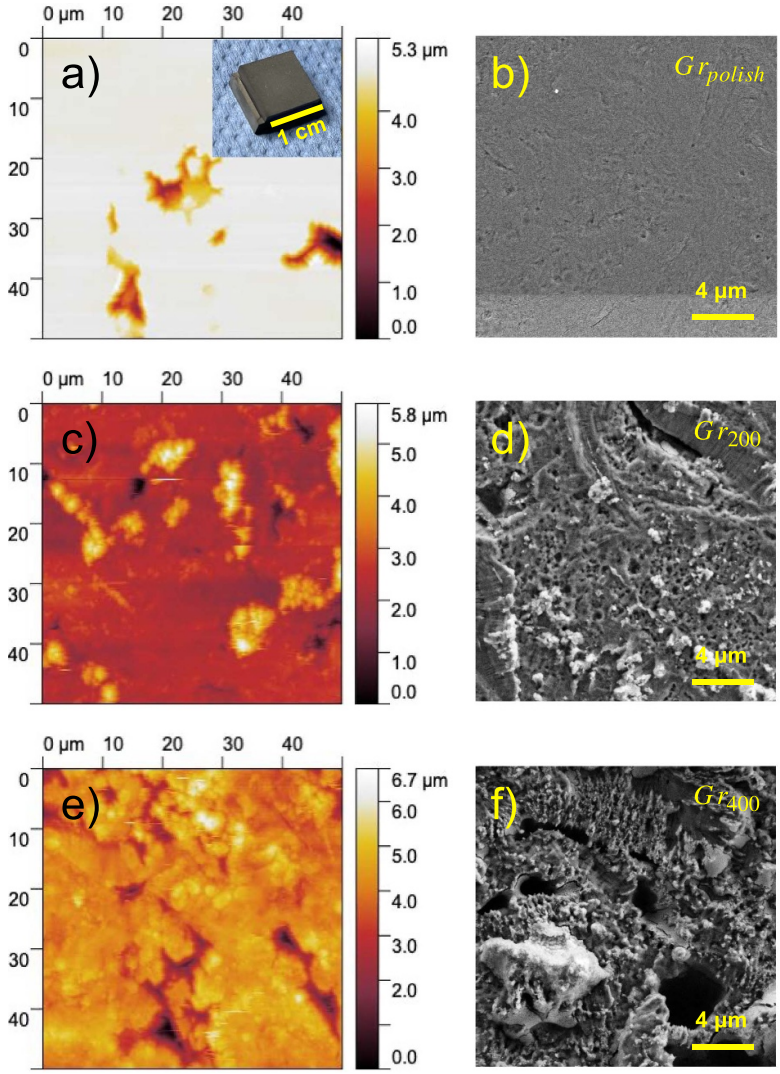

Figure 1. $50 \times 50\,\mu m^2$ AFM and SEM top-view images of: polished graphite substrates (*a*), (*b*) and plasma-etched graphite substrates with R_a of 200 nm (*c*), (*d*) and 400 nm (*e*), (*f*). Micrometric holes, consequence of the polishing procedure, can be clearly seen from AFM image (*a*). The photograph of a graphite substrate is also provided in the inset of (*a*).

source software [26]. One $20 \times 20\,\mu m^2$ AFM image was also obtained for each sample before the experiments in GyM as input for ERO2.0. A Zeiss Supra 40 high-resolution field emission scanning electron microscope (SEM), operating at an accelerating voltage of 5 kV, was used to investigate the surface structure of the specimens at both micro- and nanometer scales.

The fine-grained graphite substrates (and bulk W samples) had a 'wall footing' geometry (see the inset of figure 1(*a*)) [27]. The dimensions of the footing and the wall were $12 \times 10 \times 3$ mm^3 and $10 \times 10 \times 2$ mm^3. The 10×10 mm^2 top surface underwent a polishing procedure, during which some grains detached, resulting in micrometric holes with a coverage of approximately 10% (Gr_{polish} in the following). R_a of 100 nm and 5 nm was measured by AFM in regions with and without the holes, respectively. The surface of a subset of these substrates was etched by a plasma consisting of a carbon tetrafluoride (CF_4) and hydrogen (H_2) mixture at 9 Pa, produced with a 13.56 MHz RF power supply. Two different R_a values were obtained changing the experimental conditions. Discharge voltage of 750 V and etching time of 25 min led to a R_a of 200 nm (Gr_{200}), while 850 V and 90 min to a R_a of 400 nm (Gr_{400}) [28]. These R_a values are representative, as process-induced inhomogeneities may cause variations of ± 50 nm between samples. $50 \times 50\,\mu m^2$ AFM and SEM top-view images of fine-grained polished graphite substrates and plasma-etched graphite substrates are shown in figure 1. It is evident from SEM micrographs (*d*) and (*f*) that plasma-etching resulted in an irregular, random-like surface.

$12 \times 12 \times 0.4$ mm^3 monocrystalline N-type (Sb-doped) $\langle 100 \rangle$ silicon substrates (resistivity of 0.01–0.02 $\Omega \cdot$ cm), $R_a <$ 1 nm were also considered (Si_{flat}). Pyramids were textured on the surface of a subset of these substrates by chemical anisotropic etching [29]. Potassium hydroxide (KOH) solution was used as etchant and isopropyl alcohol (IPA) as surfactant to

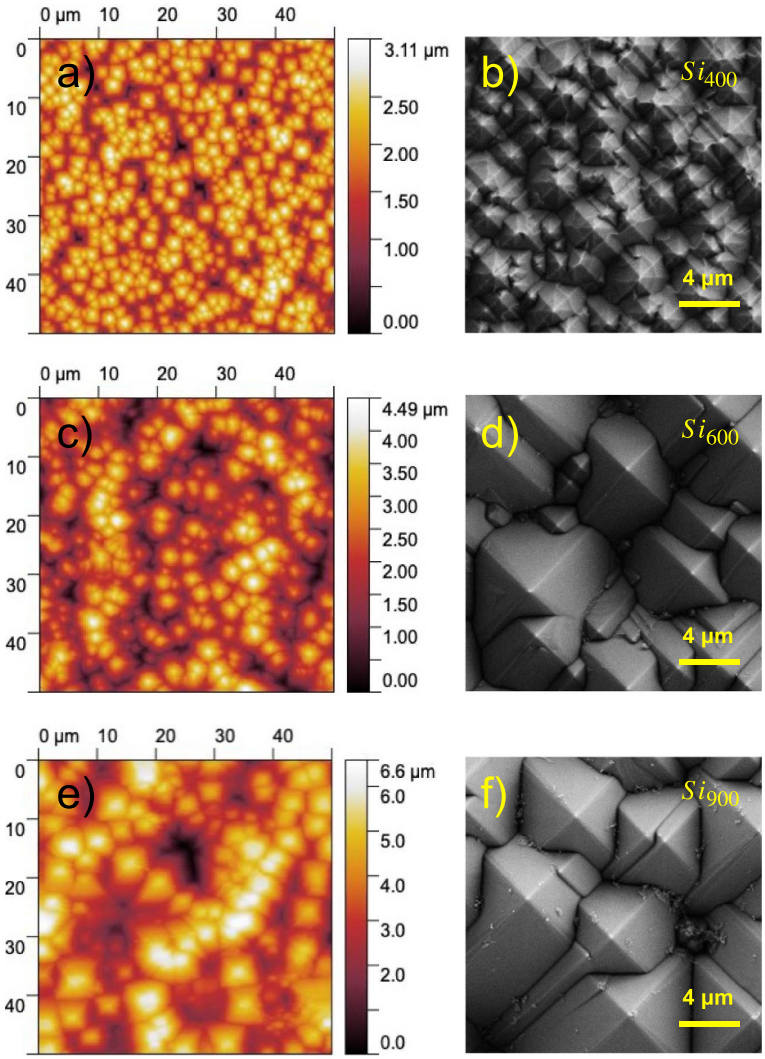

Figure 2. $50 \times 50\,\mu m^2$ AFM and SEM top-view images of anisotropically etched Si substrates with R_a of 400 nm (*a*), (*b*), 600 nm (*c*), (*d*) and 900 nm (*e*), (*f*).

improve the wettability of Si surface. Substrates with pyramids having different height were produced by adjusting the concentration of KOH, thereby controlling the etching rate: the higher the concentration, the smaller the pyramids. In particular, texturing requires a four-step procedure. (i) A 10–15 wt% aqueous KOH solution (60 ml of H_2O) was prepared in a 100 ml flask, which was placed on a magnetic hot plate stirrer. The temperature was maintained at 80 °C throughout the process. Mechanical agitation was required to keep the solution homogeneous. (ii) Three Si substrates at a time were immersed in the etching solution for 5 min to remove surface damage [30]. Then, (iii) 3 ml of IPA was added. After 7 min and 30 s, (iv) an additional 1.5 ml of the surfactant was poured into the solution to ensure sufficient wettability of the silicon surface, compensating the amount lost due to evaporation, till the end of the process, which continued for another 7 min 30 s. Figure 2 shows AFM and SEM images of the pyramid microstructure with R_a of (±50 nm) 400 nm, Si_{400} (*a*), (*b*), 600 nm, Si_{600} (*c*), (*d*), and 900 nm, Si_{900} (*e*), (*f*), produced reducing KOH concentration at stage (i) from 15 wt% to 10 wt%. SEM low-magnification micrographs (not reported here) and AFM images acquired at different regions unveiled that the surface of Si samples was completely covered by pyramids.

A compact, nanocrystalline W coating with a [110] preferential growth direction and a density close to that of bulk W was deposited on all substrates using HiPIMS [31, 32]. The thickness value of 500 nm was chosen to be high enough to survive the He plasma erosion during the exposures in GyM, but low enough to preserve the texture and roughness properties of the substrates. The variation in R_a of W-coated etched Gr and Si substrates remains within the range of 10%. AFM and SEM images of the samples as in figures 1 and 2, after W deposition, are displayed in figures 3(*a*)–(*f*), 'W/Gr', and 4(*a*)–(*f*), 'W/Si'. Micrographs of a bulk W sample (R_a of 10 nm) and a W film on a flat Si substrate (R_a of 3 nm) are also shown in figures 3(*g*)–(*h*) and 4(*g*)–(*h*), respectively.

A cross-section was prepared at the centre of the surface of the W bulk specimens by a combined high resolution field emission SEM/focused ion beam (FIB) instrument (Zeiss Crossbeam 540). Additionally, line markings were imprinted

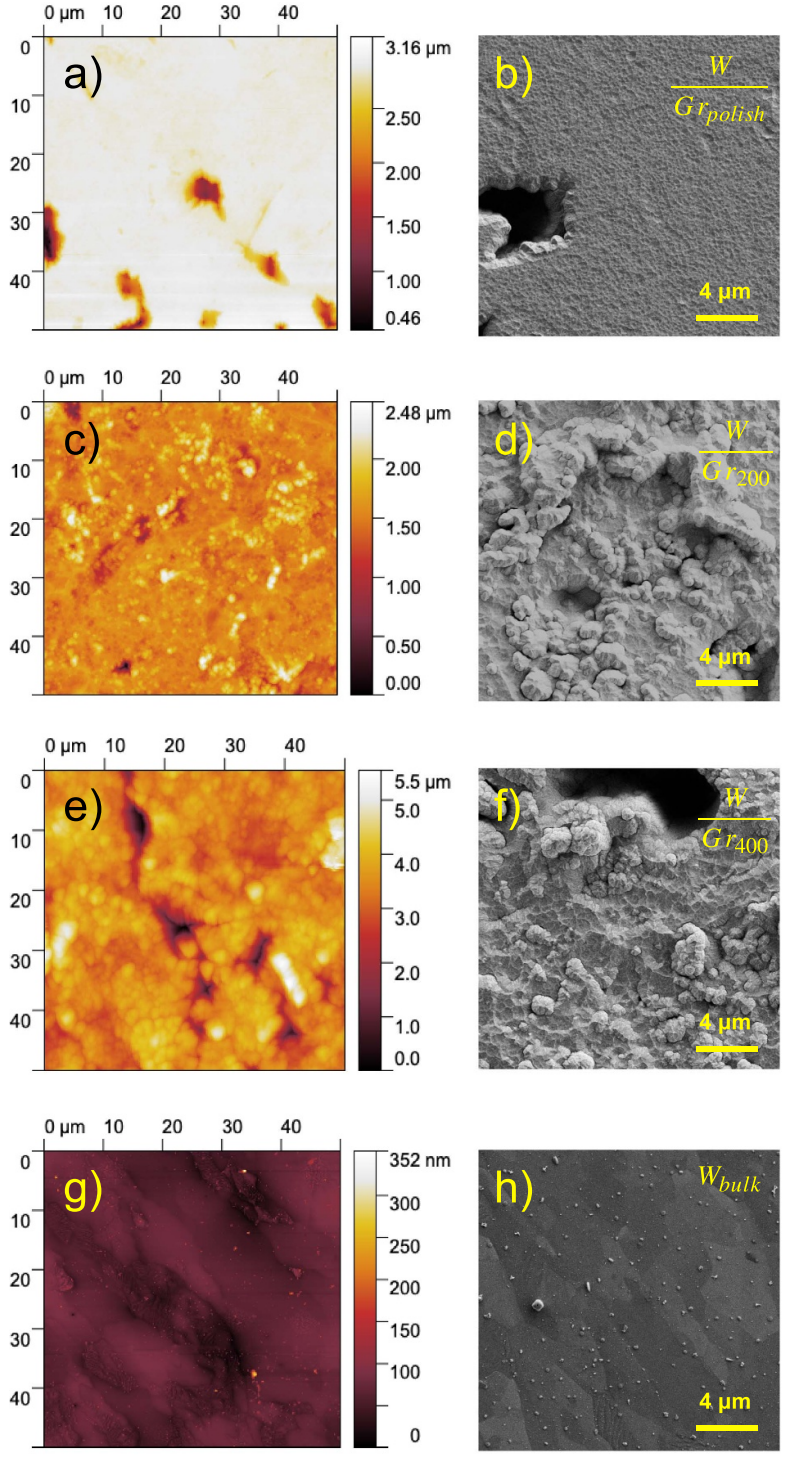

Figure 3. $50 \times 50\,\mu m^2$ AFM and SEM top-view images of the 500 nm thick W coating deposited on: polished graphite substrates (*a*), (*b*) and plasma-etched graphite substrates with R_a of 200 nm (*c*), (*d*) and 400 nm (*e*), (*f*). Micrographs of a bulk W sample are also included (*g*), (*h*).

using a 10 pA FIB beam of 30 keV gallium ions on each cross-section. The line markings, consisting of five lines spaced every 1 μm, served as distinct references for local erosion and re-deposition measurements [33].

W samples were exposed to the helium plasma of the linear device GyM, thoroughly described in [16], which can properly simulate the conditions, in terms of particle fluxes and energies, expected for the PFCs of ITER and DEMO main

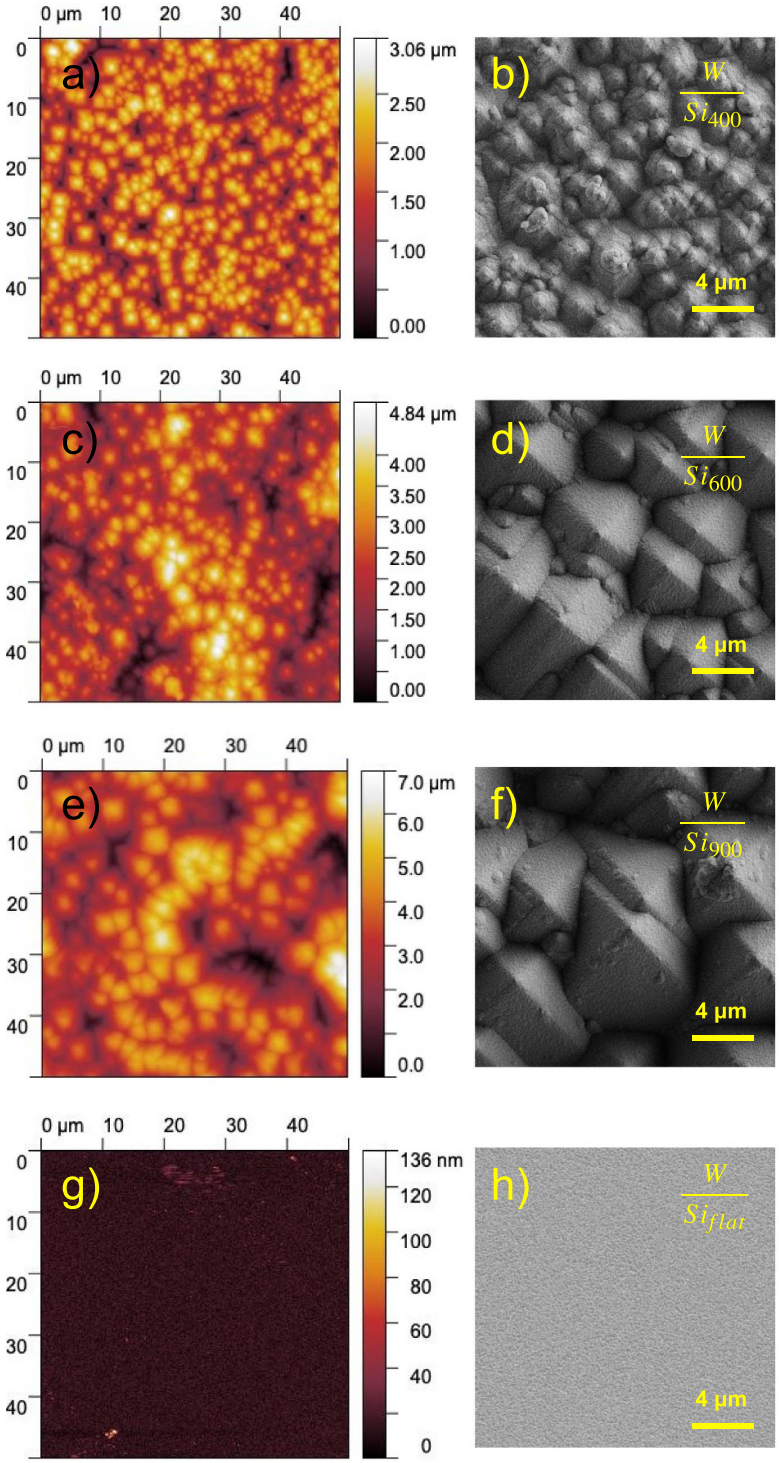

Figure 4. $50 \times 50\,\mu m^2$ AFM and SEM top-view images of the 500 nm thick W coating deposited on top of anisotropically etched Si substrates with R_a of 400 nm (*a*), (*b*), 600 nm (*c*), (*d*), 900 nm (*e*), (*f*) and on top of a Si flat substrate (*g*), (*h*).

chamber wall [17]. The layout of the experiment is depicted in figure 5(*a*), where the axial positions of the 2.45 GHz magnetron source microwave injection, the radial manipulator for material exposure and the Langmuir probe (LP) are indicated. The linear magnetic field configuration was achieved by passing a current of 600 A through the copper coils (see figures 3(*a*) and (*b*) of [16]). The sample-holder (photograph of figure 5(*a*)) is equipped with a 2 mm thick molybdenum (Mo) mask and can accommodate up to four specimens, including both W/Gr (bulk W) and W/Si geometries. The plasma-exposed area measures 10×10 mm^2. Unlike the W/Si specimens, the surface of W/Gr and bulk W samples was aligned flush with the Mo mask, as depicted in figure 5(*b*). This prevented the potential deposition of Mo atoms sputtered from the

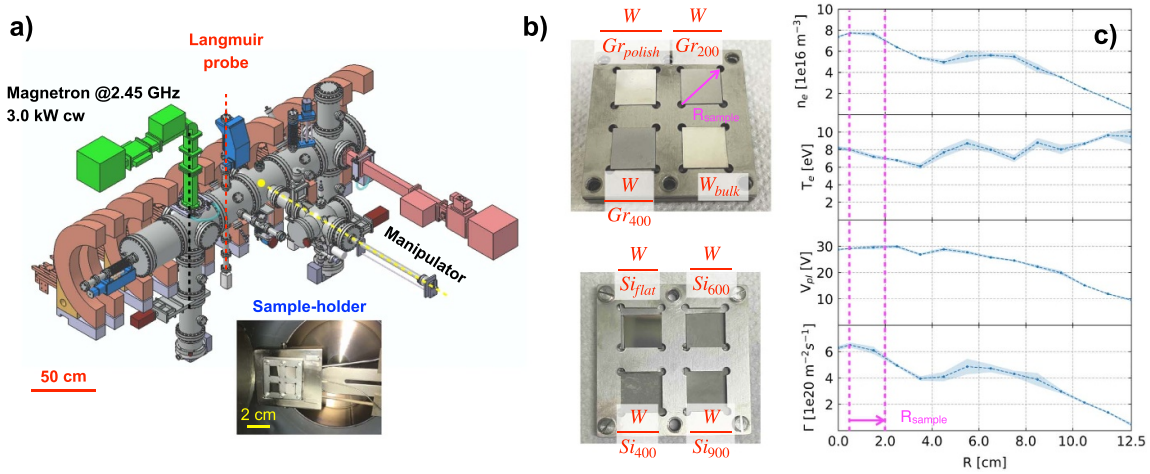

Figure 5. (*a*) Schematic of the experimental setup and photograph of the sample-holder. (*b*) Arrangement of the samples for GyM He plasma exposures. (*c*) Radial profiles of electron density, n_e, temperature, T_e, plasma potential, V_{pl}, and ion flux, Γ, from Langmuir probe data collected during one of the experiments. Each scatter point represents the average of the plasma parameter values obtained from five repeated measurements, with the shaded region indicating the associated standard deviation. The magenta arrow in (*b*) and (*c*) marks the radial extension of the samples, spanning approximately from 0.5 cm to 2 cm relative to the axis of GyM, where the centre of the sample-holder lies.

adjacent side surface of the Mo mask by the He plasma ions onto the samples. The sample-holder was oriented perpendicular to the magnetic field lines, facing toward the microwave injection sector, and positioned with its centre aligned along the axis of GyM.

The radial He plasma profiles of GyM were measured during the experiments with a cylindrical stainless steel LP (15 mm long and 1.5 mm in diameter), which was installed on a linear shift with a remote-controlled stepper motor, ≈30 cm away from the sample holder. The probe's major axis was normal to the magnetic field lines. The plasma parameters, specifically the ion flux (Γ), the electron temperature (T_e) and the density (n_e), were extracted from the LP current–voltage characteristics (*I*–*V*), following the fitting procedure described in [34]. The plasma potential (V_{pl}) was calculated from the maximum of the first derivative of *I*–*V*. GyM typically operates in the so-called sheath-limited regime [16, 35]. As a result, the plasma properties remain very similar along its axial coordinate. Therefore, the plasma profiles derived from the analysis of the LP data were assumed to be approximately the same near the sample holder.

The working pressure and magnetron power during the experiments were set at 1.0×10^{-1} Pa and 1200 W, respectively. Representative radial He plasma profiles from LP data are shown in figure 5(*c*). Due to the high reproducibility of GyM, variations in plasma parameters across different experiments conducted under the same conditions are within 10%.

Figure 5(*c*) indicates that the selected conditions enabled achieving the cut-off electron density of $\approx 7.5 \times 10^{16}$ m^{-3} at 2.45 GHz around the axis of GyM, thereby maximising the ion flux imping on the surface of the exposed samples. Furthermore, Γ remains relatively constant at $\approx 6 \times 10^{20}$ m^{-2} s^{-1} across the entire exposed surface of the specimens, radially delimited by the magenta arrow and the two dashed lines. The electron temperature profile ranges between 6 and 10 eV. These low values, combined with the low n_e, result in a low He^{2+} production probability. We may reasonably infer that the main plasma species in GyM is He^+, as also supported by the modelling work with SOLPS-ITER presented in [36].

Table 1. E_{He+} values for the plasma exposures of the W samples in GyM.

E_{He+} [eV]	W/Gr and W_{bulk}	W/Si
30		×
80		×
150	×	×
200	×	×
250	×	×
350	×	×

The W samples were exposed to the He plasma of GyM in two groups. The first set comprised the W/Gr and bulk W samples, while the second set comprised the W/Si samples (figure 5(*b*)). Exposure of the W specimens in GyM involved varying the negative bias voltage (V_{bias}) applied to the sample-holder between experiments, within the range of −320 V–0 V, in order to change the incident He^+ energy ($E_{He+} = e \cdot |V_{bias}| + e \cdot V_{pl}$, where V_{pl} is ≈30 V near the surface of the samples, figure 5(*c*)) from 30 eV to 350 eV. Each experiment lasted 2 h, resulting in a fluence of $\Gamma_{He+} \approx 4.3 \times 10^{24}$ $He^+ m^{-2}$. The E_{He+} values of the W samples' exposures are indicated in table 1.

The temperature of the specimens was measured using an Inconel-sheathed type K thermocouple (Ø = 1.0 mm), with the hot junction located behind the centre of the Mo mask [16]. The maximum recorded value during all experiments was ≈450 °C, which is well below the bulk W fuzz formation threshold $T_{th,W_{fuzz}} \approx 700$ °C [9].

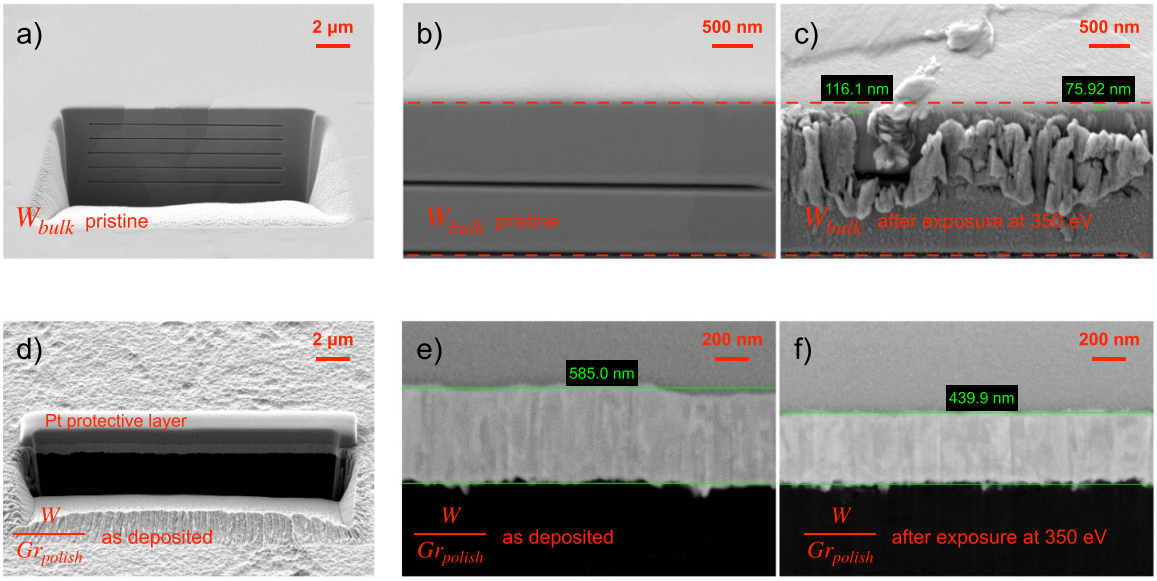

Figure 6. SEM images of FIB-prepared cross-section with line marking before (*a*), (*b*) and after bulk W sample exposure to the He plasma of GyM at $E_{He+} = 350$ eV (*c*). The red dashed lines in (*b*) and (*c*) indicate the position of the FIB marker line and the surface edge. Two values of the local erosion thickness are also reported in (*c*). SEM images of FIB-prepared cross-sections of a reference (i.e. not exposed) W/Gr_{polish} (*d*), (*e*) and of the W/Gr_{polish} exposed to the He plasma of GyM at $E_{He+} = 350$ eV (*f*). The values of the W film thickness are reported in (*e*) and (*f*). The platinum (Pt) protective layer deposited on the reference W/Gr_{polish} sample prior to FIB cross-section preparation is also labelled in (*d*).

The effects of the helium plasma exposure on the surface morphology, encompassing the topography and structure at micro- and nanometer scale, of the samples were investigated by AFM and SEM, respectively. Net erosion was assessed from mass loss data by weighing the specimens before and immediately after plasma exposure using a Sartorius SECURA225D-1S semi-micro balance with a resolution of 10 μg. Each sample was weighed five times to ensure adequate statistics. The mass loss, Δm, was determined by calculating the difference between the arithmetic means of the five measurements taken before and after the exposure. The FIB cross-sections with line markings on the bulk W specimens allowed for measuring the thickness variation via SEM to quantify local erosion and deposition (figures 6(*a*)–(*c*)). The thickness loss, Δs, was derived from the arithmetic mean of the two values reported in figure 6(*c*). For the same purpose, the SEM/FIB Zeiss Crossbeam 540 was used to estimate the thickness of a reference (i.e. not exposed) W film deposited on a polished graphite substrate and those exposed to the He plasma in GyM (figures 6(*d*)–(*f*)). Film thickness estimation was repeated twice. Similarly, a reference W/Si_{flat} sample and those exposed to the He plasma were cleaved in half, and ten cross-sectional images were acquired with the Zeiss Supra 40 high-resolution field emission SEM along the median plane. Δs for the W films deposited on polished graphite and flat silicon substrates was calculated as the difference between the arithmetic means of the SEM film thickness measurements taken on the reference samples and those obtained after the exposure. The associated error for all Δm and Δs data was determined using error propagation theory, based on the standard deviations of the repeated measurements.

3. ERO2.0 micro-scale simulations

ERO2.0 is a 3D Monte-Carlo code that simulates material erosion by a plasma, as well as the transport and deposition of released impurities, both at a global and local microscopic scale [20, 23–25]. In this work, ERO2.0 simulations incorporating the surface morphology model to account for the effect of surface roughness and texturing on the erosion of the samples exposed to the helium plasma in GyM were performed to support the interpretation of the experimental results.

$20 \times 20\,\mu m^2$ AFM images of the pristine/as deposited samples were used as input for ERO2.0, as mentioned in section 2. Specifically, for the W/Gr specimens, micrographs of regions without micrometric holes were considered. The surface topography was represented in the code by a quadrilateral mesh with surface cells of ≈100 nm per side. The simulation volume can be approximated as a parallelepiped with the sample surface on one base, an absorbing boundary on the opposite base, and periodic boundary conditions on the lateral surfaces. Sputtered particles are traced until they either exit the simulation volume or are re-deposited onto neighbouring structures.

The low density and temperature of the helium plasma in GyM resulted in a mean free path for W electron-impact ionisation of several centimetres, which is on the same order of magnitude as the characteristic dimensions of GyM. Prompt re-deposition (i.e. the process whereby sputtered impurities, ionised sufficiently close to the target material, re-deposit on the surface due to their gyro-motion around the magnetic field lines) was therefore negligible, even for particles leaving the surface at grazing angles. The low n_e and T_e also led to a

limited re-deposition of sputtered W atoms due to plasma-flow drag force, as preliminarily demonstrated by machine-sized ERO2.0 simulations [35]. For these reasons, the full dynamics of sputtered W particles was not considered in this work, and the distance between the sample surface and the absorbing boundary was set to 100 μm, helping reduce the computation time.

Regarding the other inputs for ERO2.0, the following assumptions and settings were made:

- The plasma properties in GyM remain nearly uniform along the axial coordinate, as noted in section 2. For this reason, the background plasma of electrons and He^+ ions, in which the sputtered W particles are tracked, was assumed to be uniform with n_e and T_e derived from data acquired on the machine axis by the LP located ≈30 cm from the sample holder.
- GyM exploits electron cyclotron resonance heating to sustain the plasma, and considering its low density, ions remain cold because the collisional electron-ion equipartition time is much longer than the particle lifetime [16]. The ion temperature was set to $T_i = 0.1 \cdot T_e$.
- A magnetic field of 0.08 T, parallel to the average normal of the sample surface, was considered.
- The energy of the impinging background He^+ ions was properly adjusted to account for the negative bias voltage applied to the sample holder.
- The electrostatic sheath thickness near the surface of the samples is on the order of a few hundred micrometres, which is much larger than the surface features (see the colorbar labels of the AFM images in figures 3 and 4). As a result, the sheath did not conform to the surface topology. The angle of incidence of the impinging background He^+ ions was thus assumed to be equal to the angle between the magnetic field and the cell surface normal.
- SDTrimSP calculations, which are based on the binary collision approximation (BCA) and assume an amorphous (randomised) target structure [37, 38], provided sputtering yield data as a function of the energy and incident angle of the impinging He^+ ions. These data were interpolated during the ERO2.0 simulations.
- The energy distribution of the sputtered W particles was sampled according to the Thompson distribution [39]. Their angular distribution was assumed to be a function of the impinging background He^+ ions incident angle, with a preference for the forward direction [40].

Based on the provided inputs, ERO2.0 calculated the erosion rate for each sample surface cell. Test W particles were launched until they either re-deposited onto neighbouring structures or reached the absorbing boundary in front of the sample, where they were removed from the simulation volume. Net erosion was described by the effective sputtering yield ($Y_{eff,ERO2.0}$), calculated as the number of W atoms leaving the simulation volume through the absorbing boundary divided by the flux of impinging He^+ ions. $Y_{eff,ERO2.0}$ will be directly compared to the experimental effective net erosion sputtering yield obtained from mass loss measurements ($Y_{eff,\Delta m}$).

4. Results and discussion

This section discusses the results of W sample analysis and the outcomes of related modelling efforts. Changes in the sample surface topography and structure after exposure are detailed in section 4.1. Section 4.2 presents the effective sputtering yield of bulk tungsten samples, based on both experimental data and simulations, as a function of the incident energy of He^+ ions. A comparison between Y_{eff} for samples with low average roughness is covered in section 4.3. Finally, the influence of the first moment of the surface inclination angle distribution (SIAD) on sputtering is explored in section 4.4.

4.1. Effects of helium plasma on tungsten surface morphology

Figure 7 presents the R_a values for all the samples before (squares) and after (circles) plasma exposure in GyM at the highest E_{He^+} considered, 350 eV. Figure 8 shows the SEM top-view images of bulk W, W/Gr_{polish}, W/Gr_{400}, W/Si_{flat} and W/Si_{400} samples before (*a*)–(*e*) and after (*f*)–(*l*) the same experiment. From figure 7, the surface topography does not significantly change as a consequence of the plasma irradiation, and even less so after the exposures at lower energies. Figure 8 indicates the formation of a nanoscale undulating surface structure on all the samples, which is also observed for exposures at $E_{He^+} \geqslant 250$ eV. In particular, bulk W samples developed the same nanostructures as those exposed to the helium plasma of the linear device PSI-2, below $T_{th,W_{fuzz}}$, even though the flux and fluence were much higher (2.5×10^{22} He^+m^{-2} s^{-1} and 1.0×10^{26} He^+m^{-2}, respectively) and the helium ion energy was lower (75 eV) [11, 14, 15]. The direction and spacing of the undulating surface structures are strongly influenced by each crystal grain (see figures 8(*f*) and (*k*)). There is a sharp contrast between adjacent grains, although the structure is uniform within each one. All four undulating structures described by [11, 14, 15] are present: (i) narrow interval, (ii) wide interval, (iii) jagged edge (not shown in figures 8(*f*) and (*k*)), and (iv) no undulating surface structure. The resemblance in nanostructures between results from experiments in linear devices with high fluxes and fluences at low ion energies and those with low fluxes and fluences at high ion energies has already been observed in the literature, as shown in [17, 41, 42].

In [11], electron backscattered diffraction pattern analysis was performed to elucidate the relationship between the crystal orientation of bulk W grains and the various surface structures. Specifically, it was found that grains with narrow intervals are strongly correlated with the {110}

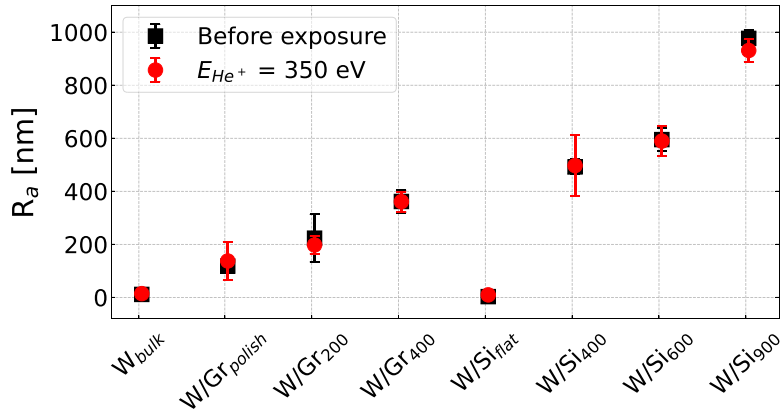

Figure 7. AFM analysis results. Average roughness R_a for all samples before (squares) and after (circles) plasma exposure in GyM at E_{He+} = 350 eV. Each scatter point represents the arithmetic mean of R_a values from three different $50 \times 50\,\mu m^2$ AFM images of the same sample, with the error bar indicating the associated standard deviation.

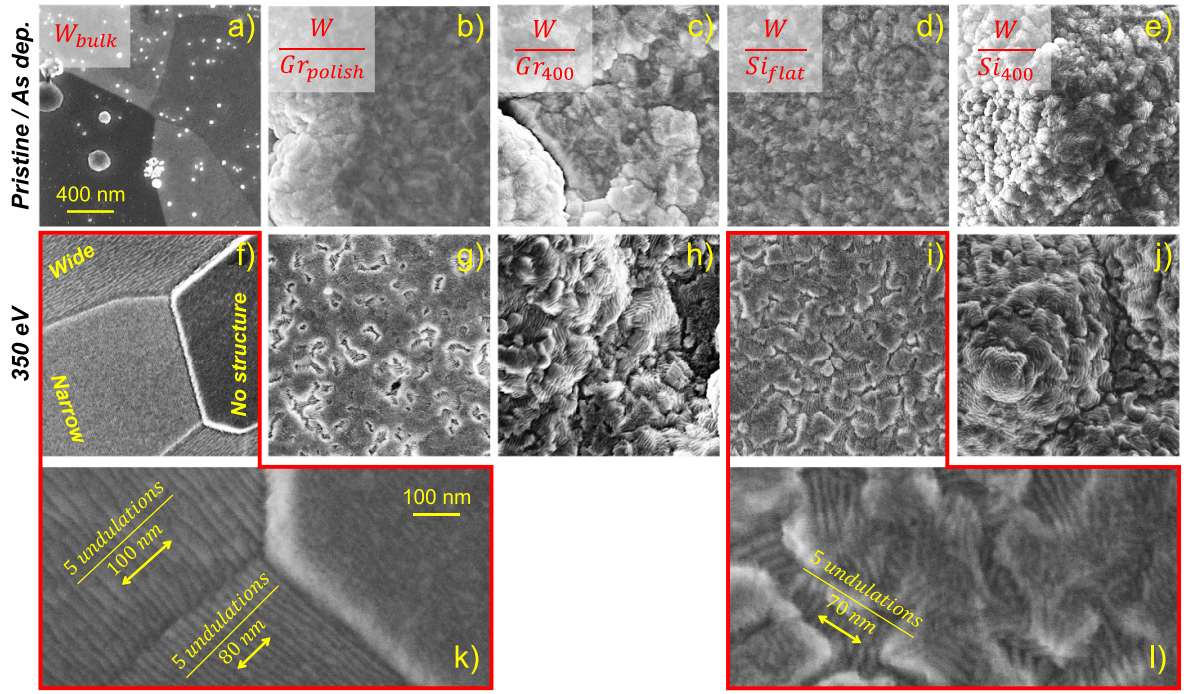

Figure 8. SEM top-view images of bulk W (*a*), (*f*), W/Gr_{polish} (*b*), (*g*), W/Gr_{400} (*c*), (*h*), W/Si_{flat} (*d*), (*i*) and W/Si_{400} (*e*), (*j*) samples, before (*a*)–(*e*) and after (*f*)–(*j*) plasma exposure in GyM at E_{He+} = 350 eV. High-magnification SEM micrographs of exposed bulk W (*k*) and W/Si_{flat} samples (*l*) are also reported.

plane. This represents the preferential crystal nanograin orientation of the HiPIMS W films examined in this study (section 2), thereby explaining why they only developed the narrow interval undulating structure (see figures 8 (*g*)–(*j*) and (*l*)).

In view of the above AFM and SEM results, the surface modifications of the samples induced by helium plasma ions are observable only at the nanoscale, which is not resolved by the ERO2.0 mesh with cells of ≈100 nm per side considered here (see section 3). Morphology evolution can therefore be deemed negligible from both an experimental and modelling point of view. This allowed for the evaluation of the quasi-static effective sputtering yield from mass loss data, as well as for running single time-step ERO2.0 simulations, thus saving computation time. The investigation of the impact of nanostructures on the W erosion, using a finer mesh in ERO2.0, represents a potential development of this work.

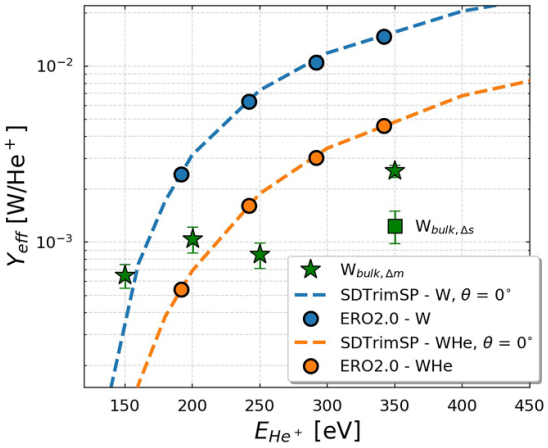

Figure 9. $Y_{\mathrm{eff},\Delta m}$ and $Y_{\mathrm{eff},\Delta s}$ of the bulk W samples as a function of the incident He^+ energy (green stars and square, respectively). $Y_{\mathrm{eff,ERO2.0}}$ is also displayed (circles), alongside SDTrimSP data (dashed lines) for He^+ ions impinging normally on the target. The compositions of the modelling surface are 100%W (blue) and 50%W50%He (orange).

4.2. Quasi-static effective sputtering yield of bulk tungsten samples

The quasi-static effective sputtering yield from the experimental mass loss was computed as follows:

$$Y_{\mathrm{eff},\Delta m}(E_{\mathrm{He^+}}) = \frac{\Delta m\ [\mathrm{g}]\ N_{\mathrm{AV}}\ [He\ \mathrm{atoms\,mol^{-1}}]}{A_{\mathrm{W}}\ [\mathrm{g\,mol^{-1}}]\ \Gamma\ [\mathrm{He^+\ ions\,s^{-1}\,m^{-2}}]\ t\ [\mathrm{s}]\ S\ [\mathrm{m^2}]} \quad (1)$$

where N_{AV} is Avogadro's number, A_{W} is the atomic weight of tungsten, t is the exposure time, S is the exposed surface area, and Γ is the He^+ ion flux derived from data acquired on the machine axis by the LP. $Y_{\mathrm{eff},\Delta m}$ of the bulk W samples as a function of the incident He^+ energy is shown in figure 9(green stars). Sputtering yield values from ERO2.0 simulations are also displayed (blue filled circles), alongside SDTrimSP data for He^+ ions impinging normally on the W target (dashed blue line) for reference. The $Y_{\mathrm{eff,ERO2.0}}$ values align with the SDTrimSP curve because the surface of the bulk W samples, with $R_{\mathrm{a}} = 10$ nm (see section 2 and figure 3(g)), is actually smooth for ERO2.0 simulations using a mesh with 100 nm cell sides.

It is clear from figure 9 that $Y_{\mathrm{eff},\Delta m}$ is generally well below the modelling predictions. The low $Y_{\mathrm{eff},\Delta m}$ values cannot be explained by prompt re-deposition or re-deposition caused by the plasma-flow drag force of W and Mo sputtered particles originating from the samples and sample-holder mask, respectively. As discussed in section 3, their impact on the effective sputtering yield was limited due to the low n_{e} and T_{e} of the helium plasma in GyM. Moreover, it is unlikely that the difference between experiment and modelling can be attributed to the LP data analysis, which has led to an overestimation of the plasma potential and ion flux, and, in turn, to an overestimation of $E_{\mathrm{He^+}}$ and an underestimation of $Y_{\mathrm{eff},\Delta m}$ by equation (1). Indeed, recent exposures of the same bulk W samples to the argon plasma in GyM have shown good agreement between $Y_{\mathrm{eff},\Delta m}$ and SDTrimSP data within a few percent.

The observed low $Y_{\mathrm{eff},\Delta m}$ relative to modelling predictions is, instead, consistent with previous findings (see [43] and references therein). Evidence from various light inert gas linear plasma device experiments suggests that the erosion rate of metals is reduced compared to standard BCA calculations and is also less than the values obtained from physical sputtering ion beam facilities, which typically operate with ion fluxes orders of magnitude lower than those in linear machine experiments. It was proposed in [43] that this discrepancy may be due to the dynamic retention of helium on the tungsten surface during plasma exposure, with this effect becoming more pronounced as the flux increases. Specifically, the local dynamic surface concentration of He results from a balance between the incoming flux and its diffusion into and out of the material. As the flux increases, the surface concentration of He correspondingly rises. This accumulation can markedly alter the surface composition. He atoms residing on the surface act to shield the underlying W lattice atoms from the momentum of incoming particles, thereby reducing their sputtering probability.

With the purpose of accounting for the dynamic retention of He in the modelling, ERO2.0 was run again (orange filled circles) using SDTrimSP data for He^+ ions impinging on a 50%W50%He mixed target [44–46]. SDTrimSP values for He^+ ions at normal incidence are also displayed (dashed orange line). Although these results are preliminary, an agreement with $Y_{\mathrm{eff},\Delta m}$ at $E_{\mathrm{He^+}} > 150$ eV is observed within a factor of two.

The FIB cross-section with line markings on the bulk W specimen exposed at the highest $E_{\mathrm{He^+}}$ of 350 eV enabled the measurement of thickness variations via SEM to quantify local erosion and deposition (see figures 6(b), (c)). The thickness loss of the specimens exposed at $E_{\mathrm{He^+}} < 350$ eV was instead below the SEM resolution of a few tens of nanometres. The sputtering yield at $E_{\mathrm{He^+}} = 350$ eV, calculated with a bulk W density of 19.25 g cm^{-3}, is shown in figure 9(green square). The factor of two difference between $Y_{\mathrm{eff},\Delta m}$ and $Y_{\mathrm{eff},\Delta s}$ can be attributed to the crystal orientation dependence of physical sputtering [47, 48]. Indeed, the micrometre-sized FIB-prepared crater samples only a limited number of grains, as illustrated in figures 6(a), (c). Thus, their average orientation may not necessarily represent the average orientation of the entire bulk W sample.

4.3. Y_{eff} of W samples with a low average roughness

The comparison of $Y_{\mathrm{eff},\Delta m}$ for samples with similar R_{a}, including bulk W, W/Si_{flat}, and W/Gr_{polish} specimens (outside the regions with holes), is presented in the bar plot of figure 10. Only $E_{\mathrm{He^+}}$ values of 250 eV and 350 eV are considered because the mass loss for W/Si samples, unlike for bulk W and W films on graphite substrates, was below the resolution limit of 10 μg of the semi-microbalance at lower incident He^+ energies. As shown in figure 10, the smaller $Y_{\mathrm{eff},\Delta m}$ for W/Si_{flat}

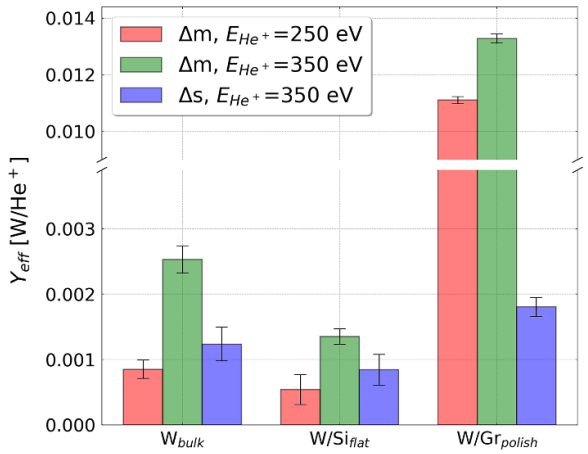

Figure 10. $Y_{\mathrm{eff},\Delta m}$ for samples with comparably low R_a: bulk W, W/Si_{flat} and W/Gr_{polish} specimens, exposed at E_{He+} of 250 eV (red bars) and 350 eV (green bars). $Y_{\mathrm{eff},\Delta s}$ for the samples exposed at E_{He+} of 350 eV is also shown (blue bars).

compared to bulk W is consistent with the $Y_{\mathrm{eff},\Delta s}$ for the exposure at $E_{He+} = 350$ eV, which was determined using the density of bulk W for the W/Si_{flat} film as well (see section 2).

The smaller $Y_{\mathrm{eff},\Delta m,\Delta s}$ values for W/Si_{flat} compared to those for bulk W can be partially explained by the different exposure geometry. As described in section 2 and shown in figure 5(*b*), the W/Gr and bulk W samples have a 'wall footing' shape, allowing their surfaces to align flush with the Mo mask of the sample holder. In contrast, the surface of the square W/Si samples was recessed by the 2 mm thickness of the Mo mask below the exposed side. Due to the low ion temperature and magnetic field values in GyM, some He^+ ions, whose guiding centre trajectories intersected near the edge of the Mo mask, may have impinged on its lateral side rather than reaching the W/Si surface because of their gyro-motion, characterised by a sub-millimetre Larmor radius. The previously mentioned physical sputtering crystal orientation dependence [47, 48] may also have contributed to the discrepancy between the $Y_{\mathrm{eff},\Delta m,\Delta s}$ values of bulk W and W/Si_{flat} samples. Indeed, they have a very different structure: the former is polycrystalline with micrometre-sized grains, while the latter consists of nanograins preferentially oriented along the [110] direction. The investigation of the role of surface structure in W erosion with the He plasma of GyM is an ongoing activity, and the results will be published in a companion paper.

It is evident from figure 10 that $Y_{\mathrm{eff},\Delta m}$ values for W/Gr_{polish} samples are significantly higher than those for bulk W and W/Si_{flat} specimens, with this trend also observed for all the other W/Gr samples. The W eroded thickness of W/Gr_{polish} specimen for the exposure at $E_{He+} = 350$ eV, calculated from the corresponding mass loss value, is approximately 1000 nm, which is twice the 500 nm thickness of the as deposited film. However, the W coating was still intact after the experiment, as can be seen from the SEM results in figures 6(*f*) and 8(*g*), and also from visual inspection. Moreover, $Y_{\mathrm{eff},\Delta s}$ from the local FIB-crater measurements is of the same order of magnitude of the values of bulk W and W/Si_{flat} samples.

A possible explanation for the high Δm values of W/Gr_{polish} and, in general, of all W/Gr samples, is related to the role of the micrometric holes covering approximately 10% of the graphite substrates surface, an inheritance from the polishing procedure (figure 1(*a*)). Indeed, W particles could have had more difficulty accessing the holes during the HiPIMS process, leading to a lower deposited film thickness, which could have been completely eroded by the He plasma, or even uncoated areas. Strong carbon physical sputtering could thus have occurred during the experiments in GyM, resulting in the high mass loss measured.

The SEM/FIB Zeiss Crossbeam 540 was used to estimate the thickness of the W film inside the graphite substrate holes for both the as deposited W/Gr_{polish} and the sample exposed to the He plasma in GyM at $E_{He+} = 350$ eV. The results are shown in figure 11. Contrary to expectations, the W coating is still intact after the experiment inside the investigated holes, and no carbon physical sputtering from the graphite substrate occurred during the experiment.

The second hypothesis for the high Δm values of the W/Gr samples and the discrepancy between $Y_{\mathrm{eff},\Delta m}$ and $Y_{\mathrm{eff},\Delta s}$ at $E_{He+} = 350$ eV for the W/Gr_{polish} specimen—currently under examination—relates to the significant temperature of ≈450 °C reached by the samples during He plasma exposure in GyM. This temperature may have led to the outgassing of impurities, such as water and carbon oxides, from the lateral uncovered sides of the porous graphite substrates during the experiments [49]. Since the weighing of the exposed samples was done immediately afterwards, the mass loss data of the W/Gr specimens may therefore reflect not only the erosion of the W film by the He^+ ions but also the removal of gases absorbed by the graphite substrates. Studying the outgassing dynamics of the W/Gr samples at ≈500 °C and assessing the potential impact of impurities on their weight could be a valuable avenue for future research.

4.4. Y_{eff} as a function of the first moment of the SIAD

Since the absolute values of $Y_{\mathrm{eff},\Delta m}$ for W/Gr and W/Si samples differ significantly, proper normalisation of the data is essential to investigate the role of topography in the sputtering of tungsten by the He plasma from GyM. Specifically, $Y_{\mathrm{eff},\Delta m}$ is normalised to $Y_{\mathrm{eff},\Delta m,W/Gr_{\mathrm{polish}}}$ for the W/Gr samples and to $Y_{\mathrm{eff},\Delta m,W/Si_{\mathrm{flat}}}$ for the W/Si samples. The obtained $Y_{\mathrm{eff},\Delta m,\mathrm{norm}}$ is displayed in figure 12 as a function of the average roughness of the specimens for the experiments at $E_{He+} = 350$ eV. Y_{eff} values from ERO2.0 simulations (assuming a 100% W surface), normalised using the same approach, are also shown. The general decreasing trend of $Y_{\mathrm{eff,norm}}$ observed in the experiments and the modelling is consistent with results from similar helium plasma exposures conducted in the PSI-2 linear device [20], involving molybdenum films deposited on the same polished and rough graphite substrates as those used in this study. However, figure 12 clearly reports that both $Y_{\mathrm{eff},\Delta m,\mathrm{norm}}$ and $Y_{\mathrm{eff,ERO2.0,norm}}$ differ for the W/Gr_{400} and W/Si_{400} samples. As explained in section 2 and shown in AFM and SEM images of figures 3 and 4, the two specimens have similar R_a but very different textures: the former has

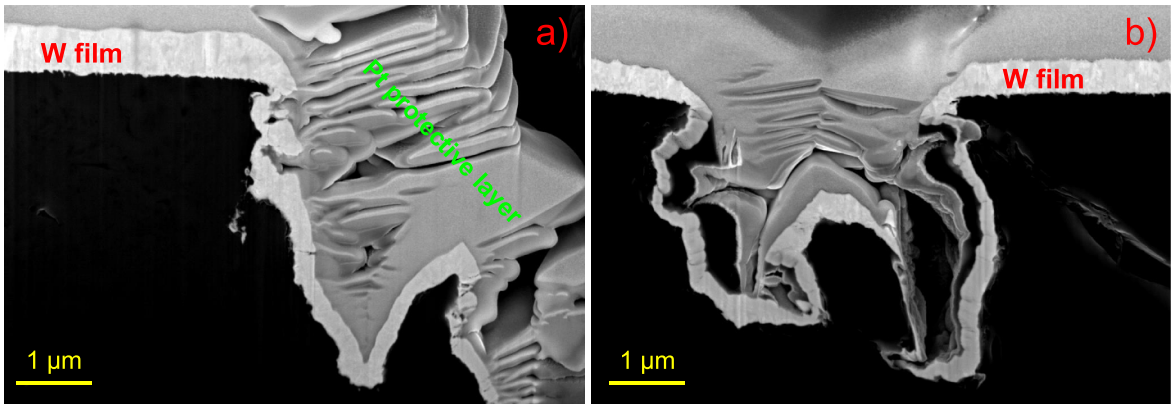

Figure 11. SEM images of FIB-prepared cross-sections in the region of graphite substrate holes of the reference W/Gr_{polish} (*a*) and the sample exposed to the He plasma in GyM at $E_{He^+} = 350$ eV (*b*).

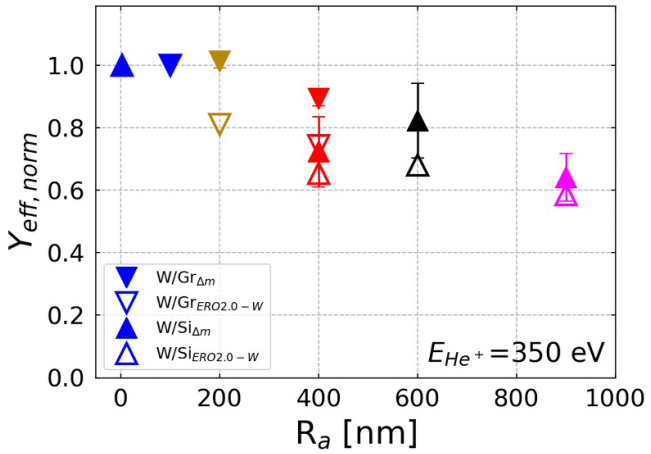

Figure 12. $Y_{\mathrm{eff},\Delta m,\mathrm{norm}}$ for the W/Gr samples (filled downward-pointing triangles) and the W/Si samples (filled upward-pointing triangles) as a function of R_a for the experiments at $E_{He^+} = 350$ eV. $Y_{\mathrm{eff,norm}}$ values from ERO2.0 simulations (assuming a 100% W surface) are also shown (open symbols).

an irregular, random-like surface (figures 3(*e*) and (*f*)), while the latter features a more regular, pyramid-like microstructure (figures 3(*a*) and (*b*)). The average roughness is therefore not suitable for characterising the sputtering behaviour of the corrugated surfaces exposed to the helium plasma in GyM.

The works [50–52] highlighted that the distribution of the surface inclination angle (δ), defined as the angle between the local surface normal and the average surface normal, is highly relevant for understanding rough surface sputtering by ion irradiation, because it is related to effects such as variation in local ion incident angles, geometrical shadowing, re-deposition, or secondary sputtering due to reflected ions. Moreover, the results reported in [21], where the erosion of W samples with roughness values ranging from the nanometer to micrometre scale was investigated using 2 keV Ar^+ ions from a mass-filtered low-flux ion source ($\approx 1 \times 10^{16}$ $Ar^+ m^{-2}$ s^{-1}), demonstrated that the first moment (or mean value) δ_m of this distribution is a very good and scale-independent parameter for characterising quasi-static sputtering of rough surfaces. For this reason, the SIAD of pristine bulk W and as deposited W/Gr and W/Si samples was obtained by post-processing all three recorded $50 \times 50\,\mu m^2$ AFM images for each specimen using the Gwyddion open-source software [26]. The results are displayed in figure 13. In this context, the average surface normal, through which δ is defined, corresponds to the direction of incidence of the He^+ ions. This is because the electrostatic sheath thickness near the surface of the samples is much larger than the surface features, as discussed in section 3.

The δ_m value for each specimen is also shown in figure 13. As expected, it is very close to zero for samples with low R_a, including bulk W, W/Si_{flat}, and W/Gr_{polish} specimens. δ_m increases with R_a for the two rough W/Gr specimens, reaching up to 23.02°, while it remains in the range of 30°–35° for the three W/Si samples with a pyramid-like microstructure. It is noteworthy that δ_m unequivocally characterises each specimen, unlike the average roughness. Specifically, δ_m is 23.02° for the W/Gr_{400} sample and 31.5° for the W/Si_{400} sample. $Y_{\mathrm{eff,norm}}$ from both mass loss data and ERO2.0 simulations is now shown in figure 14 as a function of δ_m for the exposure at $E_{He^+} = 350$ eV. Remarkably, all experimental points follow a well-defined trend despite the varying textures of the samples (see figures 3 and 4). This behaviour can be effectively fitted with a decreasing sigmoid function. $Y_{\mathrm{eff},\Delta m,\mathrm{norm}}$ remains close to 1 up to 16.53° of W/Gr_{200}, then starts to decrease, reaching a minimum value of ≈0.65 for W/Si_{900} compared to the smooth reference. The qualitative and quantitative agreement between $Y_{\mathrm{eff,ERO2.0,norm}}$ and $Y_{\mathrm{eff},\Delta m,\mathrm{norm}}$ is quite satisfactory. The simulations underestimate the experimental results by up to ≈20%. This discrepancy may stem from surface features of the samples that could have influenced the sputtering process but were not incorporated into the modelling, including the nanostructures formed after He plasma exposure (figure 8) and the micrometre holes in the W/Gr specimens. It might also result from the choice of ERO2.0 inputs, such as the energy and angular distributions of the sputtered W particles. Specifically, the energy distribution was sampled according to the Thompson distribution, while the angular

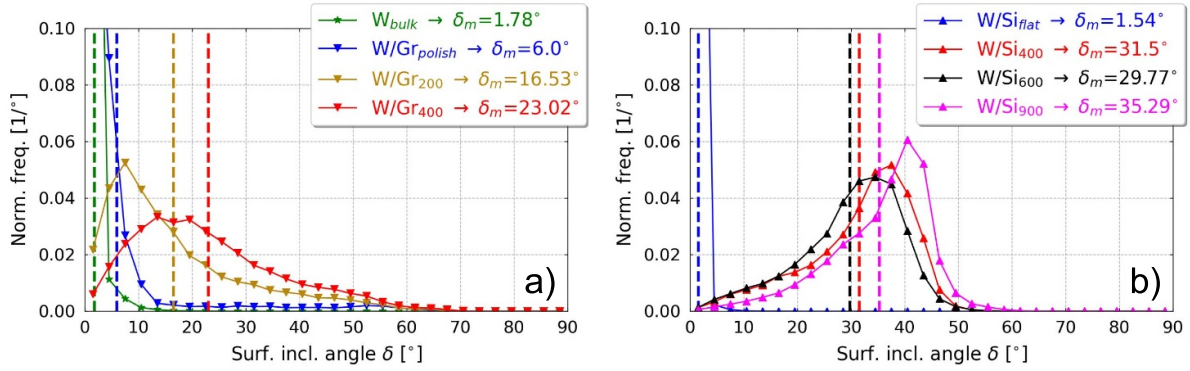

Figure 13. The distribution of the surface inclination angle δ for the pristine bulk W and reference W/Gr samples (*a*), and for the reference W/Si specimens (*b*). The first moment (or mean value) δ_m of each SIAD is indicated in the legends and by the vertical dashed lines.

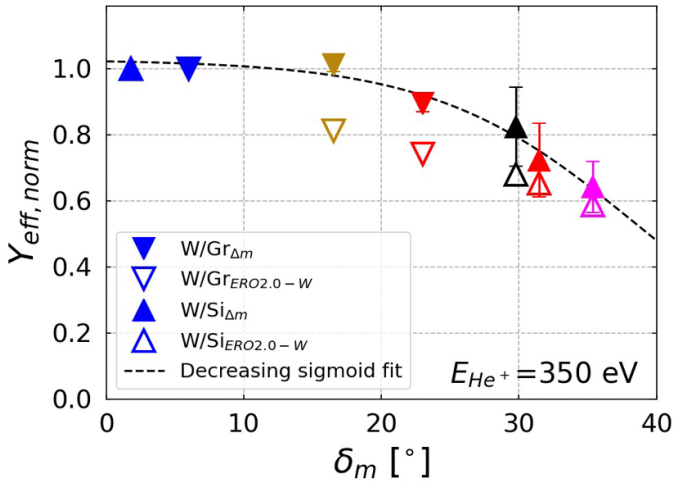

Figure 14. $Y_{\mathrm{eff},\Delta m,\mathrm{norm}}$ (filled symbols) and $Y_{\mathrm{eff,ERO2.0,norm}}$ (open symbols) for the W/Gr samples (downward-pointing triangles) and the W/Si samples (upward-pointing triangles) as a function of δ_m for the experiments at $E_{\mathrm{He}+} = 350$ eV. A decreasing sigmoid, fitted to the experimental data, is also shown (black dashed line).

distribution was modelled as a function of the incident angle of impinging He^+ ions, with a preference for the forward direction (section 3). The use of energy and angular distributions of the sputtered particles obtained from SDTrimSP runs [20] could be an option for future investigation to assess whether this improves the agreement between experiment and code outcomes. Nevertheless, ERO2.0 simulations still provide an interpretation of the behaviour of $Y_{\mathrm{eff,norm}}$ as a function of δ_m. Notably, the observed decreasing trend in $Y_{\mathrm{eff,norm}}$ with increasing δ_m is attributed to the growing fraction of sputtered W atoms being deposited on the neighbouring surfaces.

In conclusion, the first moment (or mean value) δ_m of the SIAD is effective for investigating the impact of topography on the sputtering of W samples by the He plasma of GyM. This work corroborates the results reported in [21], which, as previously mentioned, examined the erosion of W using 2 keV Ar^+ ions from an ion source. Moreover, it extends these findings to a light gas like helium, lower incident ion energies, higher ion fluxes, and a significantly different, more complex environment—namely, a linear plasma device. Furthermore, and importantly, the experimental conditions in GyM studied here are more relevant to the main chamber region of ITER and DEMO, enabling valuable considerations related to the topic of PWI in tokamaks, which will be discussed in section 5.

5. Conclusion

In this concluding section, a summary of the work is provided in section 5.1, its potential implications for tokamak PWI are discussed in section 5.2, and future developments are outlined in section 5.3.

5.1. Summary

The present work investigates the role of surface topography in the sputtering process of tungsten exposed to helium plasma, using the GyM linear device. This topic is comprehensively addressed by considering surfaces with varying roughness, ranging from the sub-nanometer scale up to ∼1 μm, as well as different textures, spanning from irregular, random-like surfaces to more regular surfaces with specific features. In particular, compact 500 nm thick tungsten (W) coatings were deposited by high-power impulse magnetron sputtering (HiPIMS)

onto graphite (Gr) substrates, which were either polished or had irregular surfaces, as well as onto silicon (Si) substrates, both flat and with pyramidal structures. The W/Gr samples included in this study featured average roughness (R_a) values of 100 nm, 200 nm, and 400 nm, while the W/Si samples had R_a values of 3 nm, 400 nm, 600 nm, and 900 nm. Polished bulk W specimens with R_a of 10 nm were also considered as reference. All specimens were exposed to the helium (He) plasma in GyM [16], with the incident He^+ energy varied between experiments in the range from 30 to 350 eV, at a fluence of $\approx 4.3 \times 10^{24}$ $He^+ m^{-2}$. The maximum temperature of the samples during all experiments was ≈450 °C, which is well below the bulk W fuzz formation threshold of ≈700 °C [9].

The effects of the helium plasma exposure on the surface morphology, encompassing the topography and structure at micro- and nanometer scale, of the samples were investigated using atomic force microscopy (AFM) and scanning electron microscopy (SEM). Global net erosion was assessed from mass loss data (Δm) obtained using a semi-micro balance. Additionally, local net erosion of bulk W specimens and W films deposited on polished graphite substrates was evaluated from thickness loss data (Δs) using FIB SEM [33]. Δs was also determined for W films deposited on flat silicon substrates from SEM cross-sectional images.

The interpretation of the experimental results was supported by simulations with 3D Monte Carlo code ERO2.0 incorporating the surface morphology model to account for the effect of surface roughness and texturing on W erosion [20, 23–25].

The main outcomes of this study can be represented schematically as follows:

- AFM images show that the surface topography of all the samples does not change significantly as a result of plasma exposure.
- SEM images indicate the formation of a nanoscale undulating surface structure on all the samples, from $E_{He^+} \geqslant$ 250 eV.
  - Bulk tungsten samples exhibited the same nanostructures as those subjected to the helium plasma in the linear device PSI-2, despite experiencing significantly higher flux and fluence levels and lower helium ion energy [11, 14, 15]. The direction and spacing of the undulating surface structures depend on the crystal grain orientation. The similarity in nanostructures between results from experiments conducted in linear devices with high fluxes and fluences at low ion energies, and those with reduced fluxes and fluences at higher ion energies, has already been observed in the literature, as documented in other papers related to GyM activities [17, 41, 42].
  - HiPIMS W films only developed a narrow interval undulating structure. This finding aligns with previous studies [11], correlating this structure with the {110} plane, which is, indeed, their preferential crystal nanograin orientation.
- The quasi-static effective sputtering yield ($Y_{eff,\Delta m}$) of bulk W and W/Si samples, derived from mass loss data, was consistently lower than the predictions from ERO2.0 and SDTrimSP models, corroborating the results from other linear device experiments [43]. This discrepancy may be attributed to the dynamic retention of helium on the tungsten surface during plasma exposure, which is not considered in the two codes. To preliminarily account for this process in the simulations, ERO2.0 was run using SDTrimSP data for He^+ ions impinging on a 50%W50%He mixed target, thereby improving the agreement between experimental and modelling results.
- $Y_{eff,\Delta m}$ values for W/Gr samples are significantly higher than those for bulk W and W/Si_{flat} specimens, while Y_{eff}, derived from thickness loss data, is of the same order of magnitude. The most credible hypothesis to explain the high Δm values for the W/Gr samples, along with the discrepancy between $Y_{eff,\Delta m}$ and $Y_{eff,\Delta s}$, is linked to the significant temperature of ≈450 °C reached by the samples during plasma exposure. This temperature may have facilitated the outgassing of impurities, such as water and carbon oxides, from the uncovered lateral sides of the porous graphite substrates during the experiments [49].
- Since the absolute values of $Y_{eff,\Delta m}$ for W/Gr and W/Si samples differ significantly, it has been normalised to enable comparison between the data from the different samples and with the ERO2.0 simulations. The first moment (or mean value) δ_m of the SIAD unequivocally characterises each specimen, unlike the average roughness. All the experimental $Y_{eff,\Delta m,norm}$ points align well with a decreasing sigmoid fit function, despite the varying R_a values and textures of the samples. The influence of surface topography on the sputtering process of tungsten exposed to GyM helium plasma can thus be captured entirely by the single parameter δ_m.
- The qualitative and quantitative agreement between $Y_{eff,ERO2.0,norm}$ and $Y_{eff,\Delta m,norm}$ as a function of δ_m is quite satisfactory. ERO2.0 indicates that the observed decreasing trend in $Y_{eff,norm}$ with increasing δ_m can be attributed to the growing fraction of sputtered W atoms being deposited on the neighbouring surfaces.

5.2. *Implications for the topic of PWI*

From the perspective of PWIs in tokamaks, the substantial quantitative difference between the experimental and modelling values of Y_{eff} underscores the critical need for accurate calibration of simulation tools such as SDTrimSP and ERO2.0 against data from linear plasma device experiments (e.g. by introducing projectile-target mixed surfaces into the model). This effort is essential for reliably predicting the lifetime of PFCs in reactors like ITER and DEMO, including those installed in the main chamber region, which will be exposed to particle fluxes in the range of 1×10^{20} to 1×10^{22} m^{-2} s^{-1} considered here. This work also highlights the structuring of the tungsten surface to increase its mean surface inclination angle as a viable approach to prolonging the lifetime of the

main chamber walls in ITER and DEMO by decreasing material erosion, which additionally provides the important benefit of reducing tungsten high-Z impurity concentration in the plasma core. To further support this statement, the exposure of other nano-engineered tungsten surfaces, such as the nano-pillar W surfaces of [53, 54], in GyM is intended.

5.3. Developments

The two primary ongoing developments to continue investigating the physics of W erosion focus on the role of surface structure, as anticipated in section 4.3, and the influence of incident particle flux. On the one hand, to study the effect of surface structure, W coatings with varying characteristics at the micro- (ranging from columnar to amorphous-like) and nano-scale (with or without a preferred growth orientation) were deposited using different techniques and then exposed to the He plasma of GyM under conditions similar to those described in this contribution. The characterisation of the samples is underway. The interpretation of the experimental results will continue to be supported by ERO2.0 simulations, incorporating new SDTrimSP data for tungsten surfaces with different crystalline orientations. On the other hand, the investigation into the influence of incident particle flux, which may play a significant role in W sputtering via dynamic retention [43], is going to be comprehensively addressed through a cross-linear plasma machine experiment involving the PSI-2 [55] and MAGNUM-PSI [56]. These two devices can achieve ion fluxes in the range of 1×10^{21}–1×10^{23} m^{-2} s^{-1} and 1×10^{23}–1×10^{25} m^{-2} s^{-1}, respectively. Together with GyM, they will allow to study a wide range of ion fluxes, spanning six orders of magnitude, from values relevant to the main chamber to those characteristic of the divertor of ITER and DEMO.

Acknowledgments

This work has been carried out within the framework of the EUROfusion Consortium, funded by the European Union via the Euratom Research and Training Programme (Grant Agreement No. 101052200—EUROfusion). Views and opinions expressed are however those of the author(s) only and do not necessarily reflect those of the European Union or the European Commission. Neither the European Union nor the European Commission can be held responsible for them. The activity has been performed under EUROfusion Work Package Plasma–Wall Interaction and Exhaust (WP-PWIE, FP9). G Alberti and M Passoni acknowledge the financial support provided by Eni SpA for their PhD program.

ORCID iDs

Andrea Uccello https://orcid.org/0000-0003-3044-1715
Gabriele Alberti https://orcid.org/0000-0001-9835-5085
Matteo Pedroni https://orcid.org/0000-0001-9391-1812
Anna Cremona https://orcid.org/0000-0001-8207-8597
Francesco Ghezzi https://orcid.org/0000-0003-3363-5187
Miriam Saleh https://orcid.org/0000-0001-5825-5012
Espedito Vassallo https://orcid.org/0000-0001-8435-4196
Luigi Bana https://orcid.org/0009-0003-1612-178X
David Dellasega https://orcid.org/0000-0002-7389-9307
Matteo Passoni https://orcid.org/0000-0002-7844-3691
Carlo Tuccari https://orcid.org/0009-0004-0144-5455
Davide Vavassori https://orcid.org/0000-0003-1279-3645
Antti Hakola https://orcid.org/0000-0003-1385-1296
Marcin Rasinski https://orcid.org/0000-0001-6277-4421
Juri Romazanov https://orcid.org/0000-0001-9439-786X

References

[1] Merola M., Escourbiac F., Raffray R., Chappuis P., Hirai T. and Martin A. 2014 *Fusion Eng. Des.* **89** 890–5
[2] Federici G., Brooks J.N., Coster D.P., Janeschitz G., Kukuskhin A., Loarte A., Pacher H.D., Stober J. and Wu C.H. 2001 *J. Nucl. Mater.* **290** 260–5
[3] Linsmeier C. *et al* 2017 *Nucl. Fusion* **57** 092007
[4] Brezinsek S. *et al* (WP PFC Contributors) 2017 *Nucl. Fusion* **57** 116041
[5] Pintsuk G. 2012 4.17—Tungsten as a plasma-facing material *Comprehensive Nuclear Materials* ed R.J. Konings (Elsevier) pp 551–81
[6] Hirai T. *et al* 2016 *Nucl. Mater. Energy* **9** 616–22
[7] Luo C., Xu L., Zong L., Shen H. and Wei S. 2023 *Fusion Eng. Des.* **190** 113487
[8] Wirth B.D., Hammond K.D., Krasheninnikov S.I. and Maroudas D. 2015 *J. Nucl. Mater.* **463** 30–38
[9] Kajita S., Sakaguchi W., Ohno N., Yoshida N. and Saeki T. 2009 *Nucl. Fusion* **49** 095005
[10] De Temmerman G., Bystrov K., Zielinski J.J., Balden M., Matern G., Arnas C. and Marot L. 2012 *J. Vac. Sci. Technol.* A **30** 041306
[11] Sakamoto R., Bernard E., Kreter A. and Yoshida N. 2016 *Nucl. Fusion* **57** 016040
[12] Bernard E. *et al* 2017 *Phys. Scr.* **T170** 014023
[13] Tsitrone E. *et al* (WEST Team) 2022 *Nucl. Fusion* **62** 076028
[14] Sakamoto R., Bernard E., Kreter A., Martin C., Pégourié B., Pieters G., Rousseau B., Grisolia C. and Yoshida N. 2017 *Phys. Scr.* **T170** 014062
[15] Sakamoto R., Bernard E., Kreter A. and Martin C. 2024 *Nucl. Fusion* **64** 036008
[16] Uccello A. *et al* 2023 *Front. Phys.* **11** 1108175
[17] Uccello A., Ghezzi F., Kovač J., Ekar J., Filipič T., Bogdanović Radović I., Dellasega D., Mellera V., Pedroni M. and Ricci D. (GyM Team) 2023 *Nucl. Mater. Energy* **35** 101422
[18] Kreter A. *et al* (The TEXTOR Team) 2008 *Plasma Phys. Control. Fusion* **50** 095008
[19] Hakola A. *et al* (The ASDEX Upgrade Team) 2014 *Phys. Scr.* **T159** 014027
[20] Eksaeva A. *et al* 2020 *Phys. Scr.* **T171** 014057
[21] Cupak C. *et al* 2021 *Appl. Surf. Sci.* **570** 151204
[22] Gaspar J. *et al* 2019 *Fusion Eng. Des.* **149** 111328
[23] Romazanov J. *et al* (JET Contributors) 2017 *Phys. Scr.* **T170** 014018
[24] Eksaeva A., Marenkov E., Borodin D., Kreter A., Reinhart M., Kirschner A., Romazanov J., Terra A., Brezinsek S. and Nordlund K. 2017 *Nucl. Mater. Energy* **12** 253–60
[25] Alberti G., Sala M., Romazanov J., Uccello A., Dellasega D. and Passoni M. 2021 *Nucl. Fusion* **61** 066039
[26] Nečas D. and Klapetek P. 2012 *Cent. Eur. J. Phys.* **10** 181–8
[27] Goriaev A. *et al* 2021 *Rev. Sci. Instrum.* **92** 023506
[28] Vassallo E. *et al* 2016 *Thin Solid Films* **603** 173–9
[29] Al-Husseini A.M. and Lahlouh B. 2017 *J. Appl. Sci.* **17** 374–83

[30] Adama K.K., Emegha J.O., Ukhurebor E.K. and Modebe L.U. 2023 *J. Mater. Eng. Struct. Comput.* **2** 1–11
[31] Dellasega D., Mirani F., Vavassori D., Conti C. and Passoni M. 2021 *Appl. Surf. Sci.* **556** 149678
[32] Vavassori D., Mirani F., Gatti F., Dellasega D. and Passoni M. 2023 *Surf. Coat. Technol.* **458** 129343
[33] Rasiński M. *et al* 2023 *Nucl. Mater. Energy* **37** 101539
[34] Desideri D. and Serianni G. 1998 *Rev. Sci. Instrum.* **69** 2354–6
[35] Mombelli F., Alberti G., Tonello E., Tuccari C., Uccello A., Baumann C., Bonnin X., Romazanov J. and Passoni M. (The GyM Team) 2025 *Nucl. Fusion* **65** 026023
[36] Alberti G., Tonello E., Carminati P., Uccello A., Bonnin X., Romazanov J., Brezinsek S. and Passoni M. 2023 *Nucl. Fusion* **63** 026020
[37] Mutzke A., Bizyukov I., Schneider R. and Davis J. 2011 *Nucl. Instrum. Methods Phys. Res.* B **269** 582–9
[38] Mutzke A., Schneider R., Eckstein W., Dohmen R., Schmid K., von Toussaint U. and Badelow G. 2019 SDTrimSP Version 6.00 *Technical Report* IPP 2019-02 (Max-Planck-Institut für Plasmaphysik Garching)
[39] Betz G. and Wien K. 1994 *Int. J. Mass Spectrom. Ion Process.* **140** 1–110
[40] Yamamura Y. 1981 *Radiat. Eff.* **55** 49–55
[41] Sala M., Uccello A., Dellasega D., Pedroni M., Vassallo E. and Passoni M. 2020 *Nucl. Mater. Energy* **24** 100779
[42] Dellasega D., Alberti G., Fortuna-Zalesna E., Zielinski W., Pezzoli A., Möller S., Unterberg B., Passoni M. and Hakola A. 2023 *Nucl. Mater. Energy* **36** 101492
[43] Doerner R.P. 2018 *Scr. Mater.* **143** 137–41
[44] Romazanov J. *et al* (JET Contributors) 2019 *Nucl. Mater. Energy* **18** 331–8
[45] Borodin D. *et al* (JET Contributors) 2019 *Nucl. Mater. Energy* **19** 510–5
[46] Romazanov J. *et al* 2022 *Nucl. Fusion* **62** 036011
[47] Schlueter K., Nordlund K., Hobler G., Balden M., Granberg F., Flinck O., da Silva T.F. and Neu R. 2020 *Phys. Rev. Lett.* **125** 225502
[48] Balden M., Schlueter K., Dhard D., Bauer P., Nilsson R., Granberg F., Nordlund K. and Hobler G. 2023 *Nucl. Mater. Energy* **37** 101559
[49] Bohdansky J., Causey R.A., Croessmann C.D., Pontau A.E. and Whitley J.B. 1989 *J. Nucl. Mater.* **162–164** 861–4
[50] Küstner M., Eckstein W., Dose V. and Roth J. 1998 *Nucl. Instrum. Methods Phys. Res.* B **145** 320–31
[51] Hu W., Dai S., Kirschner A. and Wang D. 2017 *Nucl. Mater. Energy* **12** 313–7
[52] Stadlmayr R. *et al* 2018 *Nucl. Instrum. Methods Phys. Res.* B **430** 42–46
[53] Brötzner J., Cupak C., Fellinger M., Biber H., Lopez-Cazalilla A., Granberg F., Kporha F., Mutzke A., González-Arrabal R. and Aumayr F. 2023 *Nucl. Mater. Energy* **37** 101507
[54] Gonzalez-Arrabal R., Mendez-González Y. and Perlado J.M. 2024 *Nucl. Mater. Energy* **40** 101704
[55] Kreter A., Brandt C., Huber A., Kraus S., Möller S., Reinhart M., Schweer B., Sergienko G. and Unterberg B. 2015 *Fusion Sci. Technol.* **68** 8–14
[56] Scholten J. *et al* 2013 *Fusion Eng. Des.* **88** 1785–8